Postprint of: Nitka M., Grabowski A., Shear band evolution phenomena in direct shear test modelled with DEM, POWDER TECHNOLOGY, Vol. 391 (2021), pp. 369 - 384, DOI: 10.1016/j.powtec.2021.06.025

Shear band evolution phenomena in direct shear test modelled with DEM

M. Nitka and A. Grabowski

Gdańsk University of Technology, Gdańsk, Poland

micnitka@pg.edu.pl, aleksander.grabowski@pg.edu.pl

Abstract: *A direct shear test is widely used in the geotechnical engineering field. It is an easy and quick test to measure the shear properties of soil. This test often replaces more expensive and difficult tri-axial shear test. Despite that the direct shear test is known and used for a long time, it is still not well investigated at the grain scale. This paper deals with the micro behaviour of the cohesionless sand inside the direct shear box during a geotechnical test. Numerical calculations were performed with open-source discrete code YADE. The full 3D model was used, in order to eliminate some non-physical phenomena. The numerical stress-strain curve was directly compared with the laboratory results and good agreement was obtained. The focus was on the shape of the localized zone, the properties of this zone and its behaviour. The movement of the individual grains was studied. In our analysis, the stresses were also taken into consideration. The conclusions were validated on tests with different initial void ratio (dense or loose material) and with different vertical pressure.*

Key-words: DEM, shear localization, grain-scale, direct shear

1.0 Introduction

Strain localization is one of the most important issues in granular media. The safety of engineering structures or landslides lies in the deep understanding of this phenomena. The first study on the stability of clay slopes was done by Collin [1] one hundred and seventy years ago. From an engineering point of view, the simple laboratory tests of granular media, such as oedometer, triaxial or direct shear, are most common and relevant. Usually, due to the cost and time involved, the direct shear test is performed to evaluate the soil properties. The oedometer test provides only basic parameters (not sufficient) and the tri-axial test is usually too expensive and time-consuming.

The direct shear test is known and applied for nearly one hundred years. The first modern shear box was designed by Casagrande at Harvard in 1932, and displacement control was introduced by Gilboy at MIT in 1936, which allowed the study of post-peak behaviour [2]. The advantages of the direct shear test are the simplicity of set-up and equipment used, and the ability of performing the experiment under

different saturation, drainage, and consolidation conditions [3-9]. The most important disadvantages are the size effect (boundary effect) and the strong inhomogeneity [10-13]. Deformation and stress distribution along the shear plane are highly non-uniform and the principal stresses are not known.

Despite the long history, there still exists a lack of knowledge concerning the micro-behaviour of the localization. Direct shear has widely been studied at the macroscopic level, using continuum models such as elasto-plasticity [14,15] or hypoplasticity [16].

However, for strongly discontinues, heterogeneous and non-linear granular material the discrete simulations are becoming more popular and widely used [17-24]. There are also many studies on direct shear with interface in 2D [25-32] or 3D [33-38]. In addition to numerical models, laboratory tests with PIV measurement were performed [39-41].

Though a large amount of the research was done, the formulation of the localization is not yet well recognized. Most of the papers focused on the macroscopic results or on mesoscopic, but in the residual regime. In [19], the parameters in direct shear under 3D conditions were studied, however, only 11 700 elements were used. This gives about 30 spheres in height, which could affect the localization zone. Moreover, only the post-peak behaviour was studied. A large number of spherical elements (as in our studies) were used in [20, 21], but the grain-level studies are lacking. More works focus on the interfaces [25-41], where localization forms in the area adjacent to the surface. Moreover, the studies were limited to the post-peak behaviour. In [23] the analysis of the shear localization was performed from the beginning of the test. It was limited to 2D calculations and horizontal displacements were exanimated only. The shear localization shape was studied in 3D calculations in [24]. The maps of displacements and shear stresses were presented (only in the residual part).

This article focuses mainly on the formulation of the localization at the grain level in direct shear test. This paper is a second part of the work presented in [18]. More details of the tests can be found there. Now, the emphasis was placed on displacements and rotation of grains and stresses inside the shear box in the pre-peak regime. The full 3D study was done with a real diameter of cohesionless sand, due to catch the localization phenomena. A deep understanding of the localization formulation can help to better interpret laboratory results and ensure higher safety of engineering structures (since more complex calculations are often based on soil parameters obtained from such tests).

First, the DEM model used in our approach was briefly introduced in Section 2. Then, the calibration and validation procedure was described and macroscopic results were compared with laboratory ones (Section 3). In Section 4, the sand-level results were presented, with special attention paid to the shear localization formulation. Gradients of displacements, rotations or stresses were used. Finally, a

conclusion was drawn in Section 5.

The novel points of these studies are: 1) full 3D DEM calculations, 2) real mean grain diameter of sand (a large number of elements along the height), 3) pre-peak results study at sand grain level, 4) geometric and stress studies based on the grain scale and 5) gradients analysis.

2.0 DEM method

For discrete calculations, the open-source platform YADE [42-44] was used. This model was widely used in geotechnical problem with localization [18,38,45-47]. In DEM the soil structure is composed of discontinuous grains (spheres) [48] and its main advantage is the high quality output describing the behaviour between them. In our approach, the linear contact model and spheres with contact moments were used to reduce the calculation time. Although the non-linear contact is more relevant [49,50], the differences were found negligible (less than 10%) [51].

In our calculations, only spherical elements were used. To realistically capture the particle behaviour, some rolling resistance was introduced. Such a model simulates the roughness of the particles, which is related to the non-perfect shape of the sand grains. However, this approach has several limitations, i.e. void ratio and mean coordination number may produce less realistic results in comparison with real-shape grains [52]. It was proved that the particle shape strongly affects the void-based fabric [53]. In future, work clusters of grain [54] or so-called poly-superellipsoids [55] can be used.

The model was described in details in [17,18,38,42-47]. Below only some basic equations are listed:

$$\vec{F}_n = K_n U \vec{N}, \tag{1}$$

$$\vec{F}_s = \vec{F}_{s,prev} + \Delta\vec{F}_s, \quad \text{with} \quad \Delta\vec{F}_s = K_s \Delta\vec{X}_s, \tag{2}$$

$$K_n = E_c \frac{2R_A R_B}{R_A + R_B} \quad \text{and} \quad K_s = \upsilon_c E_c \frac{2R_A R_B}{R_A + R_B}, \tag{3}$$

$$\Delta M = K_r \Delta\vec{\omega} \quad \text{with} \quad K_r = \beta K_s R_A R_B, \tag{4}$$

$$M - \eta \frac{R_A + R_B}{2} F_n \leq 0, \tag{5}$$

where U is an overlap (penetration depth) between spheres in contact (U>0 denotes contact, U = 0 if there is no contact), $\vec{N}$ is a normal vector at the contact point and $\Delta\vec{X}_s$ is the incremental tangential displacement. K_n and K_s are the normal and tangential stiffness, correlated with a modulus of elastic of

grain contact (E_c), grain radius of spheres A and B in contact (R_A and R_B) and stiffness ratio (v_c). The rolling moments ΔM depends on angular increment rotation $\Delta\vec{\omega}$, dimensionless rolling stiffness coefficient β and spheres radii. The limit of the rolling resistance is controlled by the second dimensionless coefficient η. The Coulomb condition $|F_s| \leq \mu F_n$ requires an incremental evaluation of F_s every time step, which leads to some amount of slip each time one the equalities $F_s = \pm \mu F_n$. Parameter μ denotes friction coefficient between elements.

The mechanical responses of the model are presented in Fig.1.

2.0 Model calibration and validation

The cohesionless sand was calibrated in the tri-axial test and directly compared with the experimental work of Wu [56]. Satisfactory agreement was found for both the vertical normal stress σ_1 and the volumetric strain ε_v versus vertical normal strain ε_1. Numerical tests were compared for different initial pressures (σ_0 = 50, 200 and 500 kPa). The detailed calibration was presented in [18]. The main parameters are listed in Table 1. It is worth mentioning that cohesionless sand was calibrated for the 10 times scaled sieve curve (d_{50} was equal to 5 mm, in contrast to the real sand with d_{50} equal to 0.5 mm). No shear band was present (in our calibration tri-axial test with rigid walls), thus the larger elements had a negligible influence on the macroscopic results [17]. Moreover, for the real diameter of the grains, the test would consist of more than 8 000 000 elements, which is far beyond our possibilities.

In this paper, the direct shear tests were performed with the same parameters as in [18] (calibrated in tri-axial tests). The numerical tests were simulated under full 3D conditions. In this test, the real sieve curve of Karlsruhe sand was taken into account (d_{50} = 0.5 mm) due to the localization studies. Thus, the single test consisted of more than 55 000 spheres. The model setup is presented in Figure 2. The length and height of the direct shear box were equal to 60 mm and 25 mm, respectively, as in the laboratory tests. It was proven, that the depth of the sample has a negligible effect on the results of the direct shear tests [18,45]. Therefore, it was reduced to 5 mm in order to shorten the computation time. As for the boundary condition issue, the size of a test sample must be 6 to 10 times larger than the particle size of the material being tested to avoid boundary effects [57]. The constant initial pressure σ_0 was applied to the top box. After the equilibrium state was obtained, the top box moved right (u_x) with constant velocity. The bottom part of the box was fixed throughout the calculations. A small gap

(Fig.2), corresponding to the maximum particle diameter, was created between two boxes to prevent the spheres from locking (as in the experiment). The leakage of the spheres through the gap was negligible and lower than 0.1% of the whole amount of the elements (less than 100 grains). The tests were performed under quasi-static conditions (the inertial number I was kept below 1e-4 [58]).

First, the validation of the model was checked. Note, that the DEM parameters were taken exactly the same as for calibration in the triaxial test (Tab.1). The numerical results of the sample with initial porosity e_0 = 0.63 and initial vertical pressure σ_0 = 200 kPa were compared with the experimental study of Salazar [59]. The comparison is shown in Fig. 3. Both the stress and volumetric strain were in a good agreement. The stress peak was slightly higher in the experiment (about 2.5%) and the residuum value was about 10% higher. The volumetric strain showed similar behaviour, with a smaller residuum value for the experiments. This was caused by the use of spheres instead of clumps, which provide artificial dilatancy of the material [18, 60].

It should be noted, that the material parameters were calibrated on the Karlsruhe sand in triaxial experiments, thus perfect agreement could not be obtained here. The agreement can be improved if a real grain shape would be used [61,62].

Next, the influence of the initial porosity of the sample was investigated. Samples with porosities of e_0 = 0.53, 0.63 and 0.75 were generated under a constant pressure σ_0 = 200 kPa. The different porosities were chosen to capture the spheres' behaviour under various conditions (dense, medium dense and loose, respectively). In typical DEM calculations, it is difficult to obtain void ratios outside the range e_0=0.53÷0.75 for the spherical grains. The internal friction angle φ_w and volumetric strain ε_v versus horizontal displacement u_x are presented in Fig. 4. As the void ratio increases, the internal friction angle decreases (no peak is observed for the loose specimen), but the residual value remains similar. When the initial density of the samples was dense or medium dense, dilatancy occurred almost from the beginning of the test, as in the loose sample only contraction appeared. The behaviour of the sand in the numerical calculations was similar to reality.

The influence of the initial pressure was also checked (only for medium dense samples). The internal friction angle and volumetric strain are plotted in Fig. 5. The highest internal friction angle peak and the highest stiffness were obtained for lower pressure (the residual state was the same for all specimens). Volumetric strain was the lowest for the highest pressure (with a slight contractancy at the

beginning). Again, the results were consistent with the general knowledge of the granular media behaviour.

The final localization zone was similar in all specimens (with the exception of the initially loose one [18]). The small differences were found only in the shear zone thickness [18]. The exemplary shear zone in the residual state based on grain rotation is presented in Fig. 6. The shear zone was found to be a horizontal straight line between two boxes. Its thickness varied between 18-20×d_{50}, which was in agreement with other studies [41, 63, 64].

However, the direct shear test was not homogeneous from the beginning. Not only did the material begin to shear in the middle part, but the entire specimen was mobilized. To our best knowledge, there is a gap in the study about the phenomena of the shear zone creation in a direct shear test. The next section deals with the initiation and formulation of the localization.

3.0 Shear band evolution results

So far, the research work was mainly focused on the macroscopic behaviour or sometimes on the final shape of the localization zone. There is a lack of knowledge about how the localization develops (some information is given in [24]). Usually, the shear localization is considered as a straight line (with some small fluctuations, especially when a rough interface is introduced). However, this is not the case in the direct shear. Localization tries to find the best path between the horizontal line (enforced by the boxes) and the inclined line (enforced by the natural shear angle for the granular material). This section shows the development of the localization zone in the first phase of the tests.

The figures in this articles always show initial part of the shear boxes. During the movement of the upper box, the area of interest was constant. Thus, the figures always show the region between 0 and 6 cm (the initial box size), due to visibility.

First, the fluctuations of the displacement are presented in Fig. 7. They were calculated as $\vec{u}_i - \vec{u}_{avg}$, where $\vec{u}_i$ is the displacement of *i* sphere and $\vec{u}_{avg}$ is the mean displacement of all spheres in the entire specimen. The different orientation of the arrows (or/and small values) shows the localization shape. From the early beginning of the test, the shear localization formed *s*-shape. The small values (low density) of arrows (colours) show the localization zone clearly, while grey colour shows large values of the fluctuations. Due to visibility, black arrows are presented for every 50 elements. The material showed a behaviour as for passive and active earth pressure (near the left and right boundaries,

respectively). The *s*-shape flattened during the test and the pure horizontal shear appeared well after the peak (Fig. 7f).

Since the average value of the displacement of all elements is taken, the fluctuations of the displacement are not a perfect tool for microstructure study. This method causes the information about a single grain to be fuzzy. Moreover, the fluctuations can also be calculated in a different way, which would affect the results [46,65] (e.g. mean displacement is taken only from some small region). The fluctuations were calculated only as a basis for futures studies.

In this paper, the focus was laid on the gradient values (total or normalized) of several parameters of the spheres. The gradient changes have been found as the best indicator of the variations inside the localization. It directly shows the changes in the behaviour of the granular media.

Since the results for each individual grain were too chaotic (no conclusions could be drawn), the mean value was calculated for the cuboidal REV (represent element volume). The REV had an area size of $5d_{50}\times5d_{50}$. In the third dimension, the entire specimen was taken ($10d_{50}$), because the direct shear problem is uniform in depth. Thus, about 250 grains were taken into account. The REV volume (~15.625 mm^3, ~250 grains) was chosen arbitrary, to avoid losing the grain level phenomena and to prevent chaotic behaviour of individual grains. The size of REV was already successfully used in [18,46,61]. The REV was then moved by d_{50} to obtain a better resolution of maps. All the maps are presented for u_x = 0.1 (beginning of the test), 0.5, 1.0, 1.5, 2.0 (peak), 5.0 (residual state) and 7.0 mm (end of the test). The study concentrated on the pre-peak behaviour (development of the shear zone).

First, the simple change in the position of the grains was studied (Fig.8). It was done separately for both directions – horizontal (u_x') and vertical (u_y'). The scale was defined differently for each parameter, due to its visibility. The emphasis was on the differences in the shape, not in the values. For the horizontal displacement, the blue colour corresponds to the lack of movement and the red colour corresponds to the largest displacement (Fig.8A). The white line shows the mean value, which was in agreement with the fluctuations. The mean value line also shows the place, where localization may appear. The same *s*-shaped behaviour was found, what was expected. With an increase of u_x the *s*-shape become flatter (up to the peak Fig. 8Ae) and in the residual state it was perfectly horizontal.

However, the behaviour was different when the displacement in the vertical direction was analysed (Fig.8B). Here, the red colour corresponds to the highest upwards movement and the blue colour corresponds to the highest downwards movement of spheres (maximum scale on both directions was the same). Thus, the white colour shows no vertical displacement. The concentration of the movement occurred close to both side boundaries. On the left side, where the displacement was applied, grains

moved down. The initial movement was related to the contraction caused by the shear stress. On the contrary, on the right side of the specimen, the grains moved up. For the vertical displacements, the *s*-shape did not occur. The mean values (white line) run from the upper-left corner to the bottom-right one. During the test, it flattened a bit, however, even in the residual state, it was not a straight line. Such behaviour was in contrast to the one presented with the horizontal displacement maps. Throughout the test, displacement concentrations had occurred near the boundaries. It was found quite surprising, that the vertical displacement had a completely different behaviour than the horizontal one.

For a deeper study, the gradient of displacement was calculated (Fig.9). The value of the gradient was normalized by the maximum value in each vertical strip (strip had a width equal to REV). Thus, the red colour corresponds to the highest positive increment and the blue colour corresponds to the highest negative increment in the considered vertical strip. The gradient was calculated from the bottom to the top of the shear box .

First, the gradient of the displacement in the horizontal direction (u_x*) was studied (Fig.9A). At the beginning of the test, the strong concentration appeared close to the boundaries discontinuity (near the gap between the boxes). At the left side, the inclination of the concertation was oriented downwards, differing from the right side, where it was directed upwards. The middle part of the specimen was rather chaotic (Fig.9Aa). The gradient's extremum was developed on both side of the shear box. In the middle part of the sample, maximum values created small lines, rather than a pronounced single one. Sometimes even two or three extreme values were found in one vertical strip. It shows, that the localization was not created as a uniform one, but consisted of many independent blocks. The extreme's points on the right side were still not connected to the middle ones (Fig. 9Ab). After shear displacement $u_x \geq 1.00$ mm the gradient of the horizontal displacement started to formulated one, single line, however, still it was not straight and had some minor variations (Fig. 9Ac – left part). During the test, the extremum line flattened to the completely plain one (Fig. 9Ag). At the residual state the maximum gradient was not identical in the entire specimen and some fluctuations appeared (Fig. 9Af). A conclusion is that a lot of small shear patterns are established during the test and the maximum value may appear at different heights. It seems like granular material sought for a proper path to shear, but the construction of the shear box forced it to form a straight horizontal localization at the mid-height of the specimen.

Even more interesting was a maximum gradient calculated from vertical displacements (u_y*) (Fig. 9B). After initially chaotic behaviour, the maximum of the gradient occurred close to the boundaries

discontinuity, as in the gradient's map of the horizontal direction. Moreover, a strong negative gradient was visible in the bottom-left and the top-right corners of the shear box. The maximum value inside the specimen showed a strong diagonal line not connected to the boundaries (Fig. 9Bc). Note, that inclination in this case was in contrast to the *s*-shape (although, at the beginning the *s*-shape can be found in blue colour). The behaviour of the sand was similar to the landslide slip more than to the direct shear. The angle inclination was about 33^o (the natural slope angle for sand). After $u_x \geq 1.50$ mm the maximum gradient line started to connect each other, with some small noises at the top-left and bottom-right parts (Fig. 9Bd,e). Even in the residual state, the line was not straight and still, some branching was visible (Fig. 9Bf,g). The bottom-left part was strong fluctuated during the entire test.
It's worth noting, that the neutral gradient's (white line between red and blue areas) formed similar s-shaped curve. Inside that area, grains experienced highest vertical displacements (on the left side oriented downwards and on the right side oriented upwards), connected to the dilatancy of the material.

To prove, that the final localization zone was composed of several time-depended micro localizations, the gradient of velocities is plotted (v_x and v_y) (Fig.10).The momentary behaviour is presented (velocity in a given time-step) instead of cumulative values. The behaviour was similar as for gradient in displacement, but much more fluctuated. The shape of the maximum gradient was more curved but much thinner. For example for u_x=1.00 mm, the strong *s*-shape was observed for the gradient of horizontal velocities (Fig. 10Ad) in contrast to the gradient of horizontal displacement (Fig. 9Ad). Note also, that in the residual state (Fig. 10Af,g) the maximum values changed their place and shape. Again, some discontinuities were observed. For the vertical velocities (v_y), the differences were even more significant. During the whole test, the velocities' gradient strongly varied. Up to the peak, the shape was quite similar to the gradient of displacements. Next, chaotic behaviour appeared, with maximum and minimum values placed in the middle height of the specimen (Fig10Be-g). The extreme values (before the peak in the horizontal direction and during the entire test in the vertical direction) were found not always in the middle height of the specimen, where localization was expected. It was highly non-uniform.

The gradient of the cumulative rotation and contact number was also studied (Fig. 11). Both values, rotation and contact number, are some of the most common methods to determine shear localization in DEM (or more, in granular materials). However, since the gradient was calculated, quite chaotic results were obtained before the peak for both values. After the peak ($u_x \geq 1.50$ mm) the shear localization was

more clear (Fig. 11Ad-g). No special phenomena can be found. The grain rotation was found as a result of the shearing, not as a cause.

For the contact's number gradient, the contractancy can be found in the top-left and the bottom-right parts of the specimen (Fig. 11Bb-d). Finally, the minimum of the gradient created a horizontal line in the middle of the specimen's height (Fig. 11Bf,g).

Up to now, the focus was laid on element behaviour as displacement, velocities or rolling. It was proven that the first indicator of localization appears in horizontal displacements (it was most visible from the beginning). The vertical displacements showed completely different behaviour during almost the entire test. Moreover, the rolling of spheres showed some indicators of localization rather late, and pure shear can be found at residual state only. It was proven, that the spheres rolling is not a perfect tool to mark the localization, at least in the early stage of shearing.

Finally, internal stresses were calculated and studied. The stresses were calculated by the well-known Love-Weber formula [66], [67]

$$\sigma_{ij} = \frac{1}{V^p} \sum_{c=1}^{N} x_i^c f_j^c, \tag{6}$$

where N – the number of contact points, x_i^c - the i^{th} component of branch vector jointing from the centre of mass of the particle to the contact point 'c', f_j^c - the j^{th} component of the total force at the contact point 'c' and V^p - the cell volume. The values of σ_{ij} were again calculated from an averaging cell (REV) of the size $5d_{50}\times5d_{50}\times10d_{50}$ being moved by d_{50}.

First, the gradients of normal stresses σ_{xx} (horizontal) and σ_{yy} (vertical) are presented in Fig. 12. The highest changes in gradients of the normal horizontal stresses were observed at the left part (blue colour) and the right part (red colour). The highest concentrations occurred near the moving wall (top-left) and blocked wall (bottom-right) during the pre-peak regime. The horizontal lines were visible above (blue) and below (red) the mid-part of the specimen in Fig. 12Ae. However, some oblique lines also begin to develop. In the post-peak part (Fig.12Af, g), the horizontal gradient lines connected to each other, creating a diagonal one. Although the oblique line was most significant, the horizontal stresses had a non-homogenous aspect. Still, the main changes in horizontal stresses connect top-left and bottom-right part of the box, what was in agreement with the force-chain network [18]. The displacement and stresses are not constant in the shear plane, but passive and active pressure zones appeared on the left and right side, respectively. This is in accordance with work [22-24]. However, the

final shear band was not parallel or perpendicular to the stresses paths in this case. It is consistent with recent literature, which shows that the maximal force chains are diagonal to the shear zone [20], [34], [38].

The changes in gradients for vertical stresses were different from the horizontal ones. After small shear displacement (u_x=0.50 mm) up to the end of the test, the behaviour was similar. The vertical stresses show a lot of diagonal lines with gradient's extrema (Fig.12B). The inclinations were about 60º, which corresponds to the internal friction angle of the sand. This behaviour occurred throughout the entire test, independent to the shear localization development. This behaviour was not observed in the literature, yet.

Finally, the gradients of shear stresses (σ_{xy} and σ_{yx}) are plotted (Fig. 13). From the early beginning, the maximum shear stresses occurred in the middle part of the shear box. With the height of the specimen, the shear stress increases up to the middle part and then decreases (Fig.13a-d). Such behaviour was forced by the construction of the shear box, which enforced shear localization to formulate in the middle part. However, as the test continued, the shear stresses started to deviate from the straight horizontal line due to granular media nature (13b-e). Note, that there were multiple shear locations. The inclinations of shear zones were about 30-45º and were smaller than the internal friction angle. Finally, after the peak, the changes in gradients were oblique, parallel to the gradient of the horizontal stresses. The shear stresses showed an inclination between the internal friction angle of sand and completely horizontal line forced by the shear box.

In this article, only one specimen was instigated (e_0=0.60, σ_0=200 kPa). However, similar behaviour was observed for different initial stresses (σ_0=50 kPa or 500kPa) (Fig. 14). Here, only gradients of displacement and stresses for u_x=1.00 mm were plotted.

The different behaviour was found only for the loose specimen (e_0 = 0.75). The granular media behaviour was there even more non-uniform. The behaviour was strongly affected by passive and active earth pressure boundary conditions and the shear localization was barely visible in the pre-peak regime (Fig. 15A). In the residual part, all parameters were more chaotic than for initially dense or medium dense specimen. Even the horizontal gradient of displacement did not show a straight line (Fig. 15Ba). The middle part of the specimen showed strong fluctuations through the entire test. The localization zone was more disturbed by the sand properties than by the shear box structure. Moreover,

the vertical displacement shows similar behaviour as the horizontal one (*s*-shape) in contrast to the medium dense specimen. The *s*-shape was more curved during the entire test and even in the residual state (Fig. 15B) the localization was not straight.

4.0 Conclusions

The DEM method is a powerful tool to study the micro behaviour of granular media at the grains' level. The main advantages of this article are fully 3D calculations, the real size of the sand grain, and pre-peak analysis based on geometric and stresses at grain level. After calibration, the numerical parameters can be used for different tests with a good agreement with experiments. However, better compatibility can be achieved with the use of real grain shape. The increase of computer power allows also for more and more complex calculations. The largest advantage of the discrete numerical calculations is that all micro-level phenomena can be found, in contrast to laboratory tests, where it is rather complicated, time-consuming and expensive.

The main conclusions from this paper are summarized below:

- the best indicator for the localization zone was found as horizontal displacement. It shows the localization from the very beginning of the test. However, in the pre-peak regime, the localization is not a straight line, as it would be expected. The place of the shear band is related to the internal friction angle of the sand and the construction of the direct shear box.
- The vertical displacement is unrelated to a horizontal one and shows completely different behaviour during the shear test (it is more chaotic). Its shape depends more on sand parameters (contractancy) than on shear box structure.
- The gradient of velocities shows that the shear band consist of a lot of small micro-scale localizations, which are variable over time. Those localizations after cumulation create a final shear band.
- The rotation of the spheres shows the localization rather late. It is more an effect of the shear – not the cause. A similar conclusion can be found in [18].
- The vertical stresses show the highest values between top-left and bottom-right walls of the shear box. The localization is not perpendicular or parallel to these stresses. The vertical stresses have a lot of single lines, with high inclinations above 60^{o}. That corresponds to the internal friction angle of the sand. The shear stresses show behaviour between the shear angle of sand and horizontal shear between two boxes.
- In the direct shear, the peak and residual friction angle values are a bit higher (few degrees) than in

tri-axial tests, due to the shear band shape (in direct shear test the shape is forced by the construction of the boxes, while in tri-axial it is a result of the granular media parameters only).

- In loose specimen, all above conclusions are even more relevant.

In future work, the real microstructure of granular media will be investigated (real shape and positions of the grains, based on the micro-tomography images). The results will be compared to own laboratory tests (with DIC maps). Also, cohesion between grains can be introduced since it can cause different behaviour. The same analysis can also be used for more complex geotechnical tests as biaxial or triaxial, where the position of the shear localization is not known from the beginning (in contrast to the direct shear test). Later on the real engineering problems (at a small scale, yet) can be analysed i.e. active/passive earth pressure or silo outflow.

Acknowledgments

The research work has been carried out within the project "*Autogenous coupled dynamic-acoustic effects in granular materials - experiments and combined DEM/CFD approach*" financed by the National Research Centre (NCN) (UMO-2017/27/B/ST8/02306) and "*Numerical analysis of the shear zone between granular material and corrugated sheet in DEM and MPM codes*" financed by the Gdańsk University of Technology, Poland (*Grant for Young Researchers* – no. 034628).

Bibliography

[1] Skempton A.W., Aleksander Collin: a note on his pioneer work in soil mechanics, *Geotechnique* 1, 216 (1949)

[2] Matthews M. C., The engineering application of direct and simple shear testing, *Ground Enging* 21, No. 2, 13–21 (1988)

[3] Schwedes, J., Testers for measuring flow properties of particulatesolids, *Powder Handling and Processing* 12, 337–385 (2000)

[4] Potyondy J.G., Skin friction between various soils and construction materials, *Geotechnique* 4, 339–353 (1961)

[5] Desai C.S., Drumm E.C., Zama, M.M., Cyclic testing and modeling of interfaces, *Journal of Geotechnical Engineering ASCE* 111(6) (1985)

[6] Jewell R.A., Wroth C.P., Direct shear tests on reinforced sand, *Geotechnique* 37(1), 53–68 (1987)

[7] Tejchman J., Wu W., Experimental and numerical study of sand-steel interfaces, *International*

Journal of Numerical and Anal. Methods in Geomechanics 19(8), 513–537 (1995)
[8] Shibuya S., Mitachi T., Tamate S., Interpretation of direct shear box testing of sands as quasi-simple shear, *Geotechnique* 47, 769–790 (1997)
[9] Chandler R.J., Hamilton P.S., On the measurement of the undrained strength of discontinuities in the direct shear box, *Geotechnique* 49(5), 615–620 (1999)
[10] Terzaghi K., Peck R.B., Soil mechanics in engineering practice, *Wiley, New York* (1948)
[11] Saada A.S., Townsend F.C., State of the art: laboratory strength testing of soils. Laboratory shear strength of soil, *A STM Special Technical Publishing* 740, 7–77 (1981)
[12] Scarpelli G., Wood D.M., Experimental observations of shear band patterns in direct shear test, *Proceedings of IUTAM Conference on Deformation and Failure of Granular Materials, Delft,* 473–484 (1982)
[13] Uesugi M., Kishida H.: Influential factors of friction between steel and dry sand, *Soils and Foundations* 26(2), 33–46 (1986)
[14] Frydman S. and Talesnick M., Simple shear of isotropic elasto–plastic soil, *Numerical and Analytical Methods in Geomechanics* (15), 251-270 (1991)
[15] Gutierrez M., Wang J., Yoshimine M., Modeling of the simple shear deformation of sand: effects of principal stress rotation, *Acta Geotechnica* 3, 193-201 (2009).
[16] Tejchman J. and Bauer E., FE-simulations of a direct and a true simple shear test within a polar hypoplasticity, *Computers and Geotechnics* 32(1), 1-16 (2005)
[17] Kozicki J., Niedostatkiewicz M., Tejchman J., Mühlhaus H.-B., Discrete modelling results of a direct shear test for granular materials versus FE results, *Granular Matter 15*(5), 607-627 (2013)
[18] Grabowski A., Nitka M., 3D DEM simulations of basic geotechnical tests with early detection of shear localization. *Studia Geotechnica Et Mechanica*, https://doi.org/10.2478/sgem-2020-0010 (2020)
[19] Cui L., O'Sullivan C., Exploring the macro- and micro-scale response of an idealised granular material in the direct shear apparatus, *Géotechnique* 56 (2006)
[20] Salazar A., Sáez E., Pardo G., Modeling the direct shear test of a coarse sand using the 3D Discrete Element Method with a rolling friction model, *Computers and Geotechnics* 67, 83-93 (2015)
[21] Bernhardt M. L., Biscontin G., O'Sullivan C., Experimental validation study of 3D direct simple shear DEM simulations, *Soils and Foundations* 56, 336-347 (2016)
[22] Wang C., Deng A., Taheri A., Three-dimensional discrete element modeling of direct shear test for granular rubber–sand, *Computers and Geotechnics* 97, 204-216 (2018)
[23] Zhou Q., Shen H., Helenbrook B., Zhang H.W., Scale dependence of direct shear tests, *Chinese*

Science Bulletin 54, 4337-4348 (2009)
[24] Wang, J., Dove, J. E., Gutierrez, M. S., Discrete-continuum analysis of shear banding in the direct shear test, *Geotechnique* 57 (6), 513–526 (2007)
[25] Jensen R.P., Bosscher P.J., Plesha M.E., Edil T.B., DEM simulation of granular media-structure interface: effects of surface roughness and particle shape, *Int. J. Numer. Anal. Meth. Geomech*. 23(6), 531–547 (1999)
[26] Frost J.D., Dejong J.T., Recalde M., Shear failure behavior of granular-continuum interfaces, *Eng. Fract. Mech.* 69 (17), 2029-2048 (2002)
[27] Frost J.D., DeJong J.T., In situ assessment of role of surface roughness on interface response, *J. Geotech. Geoenviron. Eng*. 131 (4), 498–511 (2005)
[28] Wang J., Gutierrez M.S., Dove J.E., Numerical studies of shear banding in interface shear tests using a new strain calculation method, *Int. J. Numer. Anal. Meth. Geomech*. 31 (12), 1349-1366 (2007)
[29] Wang J., Jiang M., Unified soil behavior of interface shear test and direct shear test under the influence of lower moving boundaries, *Granular Matter*, doi: 10.1007/s10035-011-0275 (2011)
[30] Gu X., Chen Y., Huang M., Critical state shear behavior of the soil-structure interface determined by discrete element modelling, *Particuology*, 35, 68-77 (2017)
[31] Zhu H., Zhou W.H., Yin Z.Y., Deformation mechanism of strain localization in 2D numerical interface tests, *Acta Geotechnica* 13(3), 557-573 (2018)
[32] Jing X.Y., Zhou W.H., Li Y., Interface direct shearing behavior between soil and saw-tooth surfaces by DEM simulation, *Procedia Engineering* 175, 36-42 (2017)
[33] Jing X. Y., Zhou, W. H., Zhu, H. X., Yin, Z. Y., Li, Y., Analysis of soil-structural interface behavior using three-dimensional DEM simulations, *International Journal for Numerical and Analytical Methods in Geomechanics* 42(2), 339-357 (2018)
[34] Feng S.J., Liu X., Chen H.X., Zhao T., Micro-mechanical analysis of geomembrane-sand interactions using DEM, *Computers and Geotechnics* 94, 58-71 (2018)
[35] Zhou W. H., Jing X. Y., Yin Z. Y., Geng X. Effects of particle sphericity and initial fabric on the shearing behavior of soil-rough structural interface, *Acta Geotechnica*, 14(6), 1699-1716 (2019)
[36] Zhang N., Evans T.M., Three dimensional discrete element method simulations of interface shear, *Soils and Foundation*s 58(4), 941-956 (2018)
[37] Xue-Ying J., Wan-Huan Z., Yangmin L., Interface direct shearing behavior between soil and saw-tooth surfaces by DEM simulation, *Procedia Engineering* 175, 36-42 (2017)
[38] Grabowski A., Nitka M., Tejchman J., 3D DEM simulations of monotonic interface behaviour

between cohesionless sand and rigid wall of different roughness, *Acta Geotechnica*, doi: 10.1007/s11440-020-01085-6 (2020)
[39] De Jong J.T., Randolph M.F., White D.J., Interface load transfer degradation during cyclic loading: a microscale investigation, *Soils Found* 43(4), 81–93 (2003)
[40] De Jong J.T., White D.J., Randolph M., Microscale observation and modeling of soil-structure interface behavior using particle image velocimetry, *Soils Found* 46(1), 15–28 (2006)
[41] De Jong J.T., Westgate Z.J., Role of initial state, material properties, and confinement condition on local and global soil– structure interface behaviour, *J Geotech Geoenviron Eng* 135(11), 1646-1660 (2009)
[42] Kozicki J., Donze, F.V., A new open-source software developed for numerical simulations using discrete modelling methods, *Computer Methods in Applied Mechanics and Engineering* 197, 4429-4443 (2008)
[43] Kozicki J., Donze F.V., Yade-open dem: an open-source software using a discrete element method to simulate granular material, *Engineering Computations* 20, 786-805 (2008)
[44] Šmilauer V., Chareyre B., Yade DEM Formulation. *Manual* (2011)
[45] Kozicki J., Niedostatkiewicz M., Tejchman J., Mühlhaus H.-B., Discrete modelling results of a direct shear test for granular materials versus FE results, *Granular Matter* 15(5), 607-627 (2013)
[46] Nitka M., Tejchman J., Kozicki J., Leśniewska D., DEM analysis of micro-structural events within granular shear zones under passive earth pressure conditions, *Granular Matter* 3, 325-343 (2015)
[47] Danuta L., Nitka M., Tejchman-Konarzewski A., Pietrzak M.: Contact force network evolution in active earth pressure state of granular materials: photo-elastic tests and DEM, *Granular Matter*, 22-71 (2020)
[48] Cundall P. A., Hart R., Numerical modeling of discontinua, *J. Eng. Comp.* 9, 101–113 (1992)
[49] Hertz H., On the contact of elastic solids, *J. Reine und Angewandte Mathematik* 92, 156-171 (1882)
[50] Mindlin R.D., Deresiewicz H., Elastic spheres in contact under varying oblique forces, *J. Appl. Mech. Trans. A.S.M.E.* 75, 327-344 (1953)
[51] Yeom, S.B, Ha, E.-S., Kim, M.-S., Jeong. S.H., Hwang, S.-J., Choi, D.H., Application of the discrete element method for manufacturing process simulation in the pharmaceutical industry, *Pharmaceutics* 11(8), 414 (2019)
[52] Zhao S., Evans T.M., Zhou X., Shear-induced anisotropy of granular materials with rolling resistance and particle shape effects, *International Journal of Solids and Structures* 150 (1), 268-281

(2018)
[53] Zhao S., Evans T. M., Zhou X., Three-dimensional voronoi analysis of monodisperse ellipsoids during triaxial shear, *Powder Technology* 323, 323–336 (2018b)
[54] Kozicki J., Tejchman J. and Mróz Z., Effect of grain roughness on strength, volume changes, elastic and dissipated energies during quasi-static homogeneous triaxial compression using DEM, *Granular Matter* 14 (4), 457-468 (2012)
[55] Zhao S., Zhao J., A poly-superellipsoid-based approach on particle morphology for DEM modeling of granular media, *Int J Numer Anal Methods Geomech*, 1-13 (2019)
[56] Wu W., Hypoplastizität als mathematisches Modell zum mechanischen Verhalten granularer Stoffe, *Heft 129, Institute for Soil- and Rock-Mechanics, University of Karlsruhe* (1992)
[57] ASTMD3080/D3080M-11. Standard Test Method for Direct Shear Test of Soils Under Consolidated Drained Conditions, *ASTM International, West Conshohocken* (2011).
[58] Roux J.-N., Chevoir F., Discrete numerical simulation and this mechanical behavior of granular materials, *Bulletin des Laboratoires des Ponts et Chaussees* (2005).
[59] Salazar A., Sáez E., Pardo G., Modeling the direct shear test of a coarse sand using the 3D discrete element method with a rolling friction model, *Computers and Geotechnics* 67, 83-93 (2015)
[60] Zhao S., Evans T.M., Zhou X., Shear-induced anisotropy of granular materials with rolling resistance and particle shape effects, *International Journal of Solids and Structures*, 150, 268-281 (2018)
[61] Nitka M., Tejchman J., A three-dimensional meso scale approach to concrete fracture based on combined DEM with X-ray μCT images, *Cement and Concrete Research* 107, 11-29 (2018)
[62] Kawamotoa R., Andò E., Viggiani G., Andrade J.E., All you need is shape: Predicting shear banding in sand with LS-DEM, *Journal of the Mechanics and Physics of Solids* 111, 375-392 (2018)
[63] Tejchman J., Scherzonenbildung und Verspannungseffekte in Granulaten unter Berücksichtigung von Korndrehungen, *Publ. Ser. Inst. Soil and Rock Mech., University Karlsruhe* 117, 1-236 (1989)
[64] Tejchman J., Wu W., Experimental and numerical study of sand-steel interfaces, *Int. J. Numer. Anal. Methods Geomech*. 19(8), 513-537 (1995)
[65] Kozicki J., Tejchman J., Investigations of quasi-static vortex structures in 2D sand specimen under passive earth pressure conditions based on DEM and Helmholtz-Hodge vector field decomposition, *Granular Matter* 19, 19-31(2017)
[66] Christoffersen J., Mehrabadi M.M., S. Nemat-Nasser S., A Micromechanical Description of Granular Material Behavior, *J. Appl. Mech*. 48(2), 339-344 (1981)

[67] Luding S., Micro-macro transition for anisotropic, frictional granular packings, *International Journal of Solids and Structures* 41, 5821-5836 (2004)

List of tables and figures

Fig.8: Evolution of displacements: A) u_x' (horizontal) and B) u_y' (vertical) in the entire specimen for: a) u_x=0.1 mm, b) u_x=0.50 mm, c) u_x=1.00 mm, d) u_x=1.5 mm, e) u_x=2.0 mm, f) u_x=5.0 mm and g) u_x=7.0 mm (red colour denotes positive displacement, blue colour denotes negative displacement) *(colour online)*

Fig.9: Evolution of the gradient of displacements: A) u_x* (horizontal) and B) u_y* (vertical) in the entire specimen for: a) u_x=0.10 mm, b) u_x=0.50 mm, c) u_x=1.00 mm, d) u_x=1.50 mm, e) u_x=2.00 mm, f) u_x=5.00 mm and g) u_x=7.00 mm (blue colour denotes increase, red colour denotes decrease) *(colour online)*

Fig.10: Evolution of gradient of velocities: A) v_x (horizontal) and B) v_y (vertical) in the entire specimen for: a) u_x=0.10 mm, b) u_x=0.50 mm, c) u_x=1.00 mm, d) u_x=1.50 mm, e) u_x=2.00 mm, f) u_x=5.00 mm and g) u_x=7.00 mm (red colour denotes increase, blue colour denotes decrease) *(colour online)*

Fig.11: Evolution of gradient of A) rolling and B) contact number in the entire specimen for: a) u_x=0.10 mm, b) u_x=0.50 mm, c) u_x=1.00 mm, d) u_x=1.50 mm, e) u_x=2.00 mm, f) u_x=5.00 mm and g) u_x=7.00 mm (red colour denotes increase, blue colour denotes decrease) *(colour online)*

Fig.12: Evolution of gradient of stresses A) σ_{xx} and B) σ_{yy} in the entire specimen for: a) u_x=0.10 mm, b) u_x=0.50 mm, c) u_x=1.00 mm, d) u_x=1.50 mm, e) u_x=2.00 mm, f) u_x=5.00 mm and g) u_x=7.00 mm (red colour denotes increase, blue colour denotes decrease) *(colour online)*

Fig.13: Evolution of gradient of stresses A) σ_{yx} and B) σ_{yx} in the entire specimen for: a) u_x=0.10 mm, b) u_x=0.50 mm, c) u_x=1.00 mm, d) u_x=1.50 mm, e) u_x=2.00 mm, f) u_x=5.00 mm and g) u_x=7.00 mm (red colour denotes increase, blue colour denotes decrease) *(colour online)*

Fig.14: Maps of gradient for specimen with initial pressure equal: A) σ_0 = 50 kPa and B) σ_0 = 500 kPa for entire specimen for u_x=1.00 mm: a) horizontal displacement (u_x*) b) vertical displacement (u_y*), c) horizontal stresses (σ_{xx}), d) vertical stresses (σ_{yy}), e) shear stresses (σ_{xy}) and f) shear stresses (σ_{yx}) (red colour denotes increase, blue colour denotes decrease) *(colour online)*

Fig.15: Maps of gradient for initial loose specimen (e_0=0.75) for entire specimen for A) u_d=1.00 mm (pre-peak) and B) u_d=5.00 mm (residual part): a) horizontal displacement (u_x*) b) vertical displacement (u_y*), c) horizontal stresses (σ_{xx}), d) vertical stresses (σ_{yy}), e) shear stresses (σ_{xy}) and f) shear stresses (σ_{yx}) (red colour denotes increase, blue colour denotes decrease) *(colour online)*

Table 1. Material micro-parameters for discrete simulations

Material micro-parameters	Value
Modulus of elasticity of grain contact E_C (MPa)	300
Normal/tangential stiffness ratio of grain contact v_C (−)	0.3
Inter-particle friction angle μ (º)	18
Rolling stiffness coefficient β (−)	0.7
Moment limit coefficient η (−)	0.4

TABLE 1

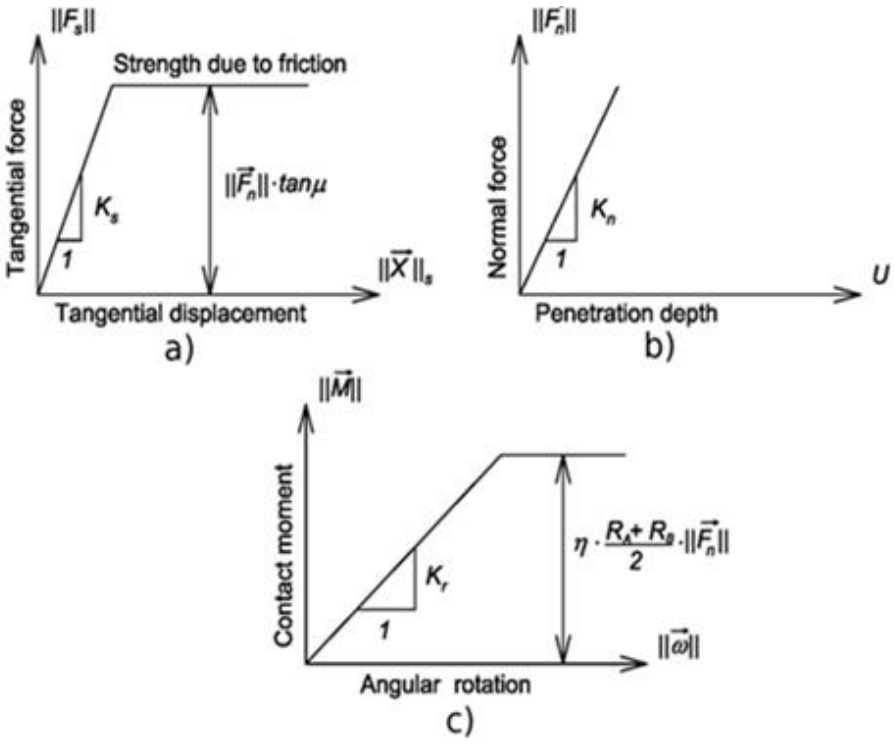

Fig.1: Mechanical response of (a) tangential (b) normal and (c) rolling contact model laws [42]

FIGURE 1

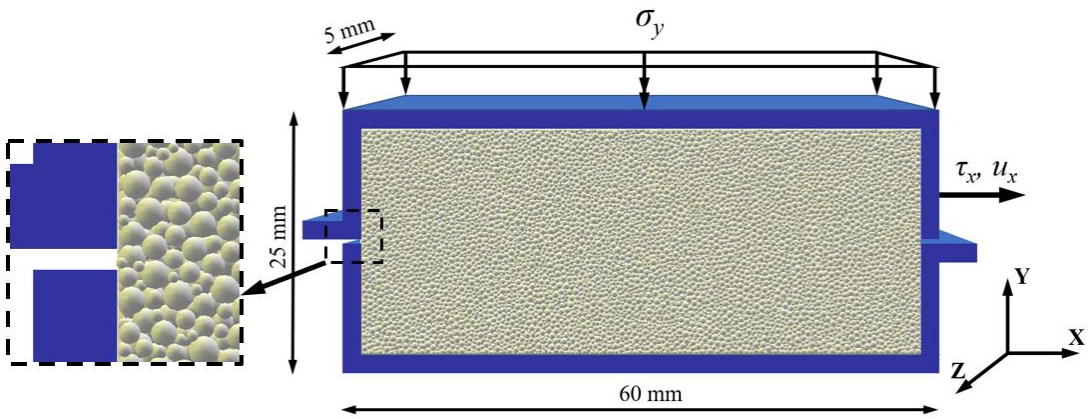

Fig. 2: Model set-up for numerical simulations of direct shear test with the zoom on the gap between boxes

FIGURE 2

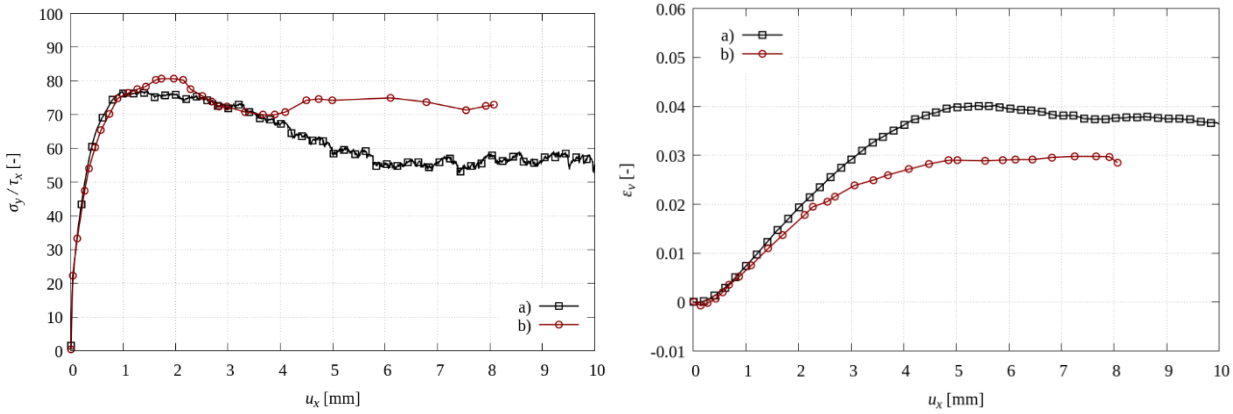

Fig. 3: Stress ratio σ_0/τ_x and strain ε_v versus horizontal displacement u_x from direct shear test for: a) numerical simulations and b) laboratory test of Salazar et al [59] (e_0 = 0.63 and σ_0 = 200 kPa)

FIGURE 3

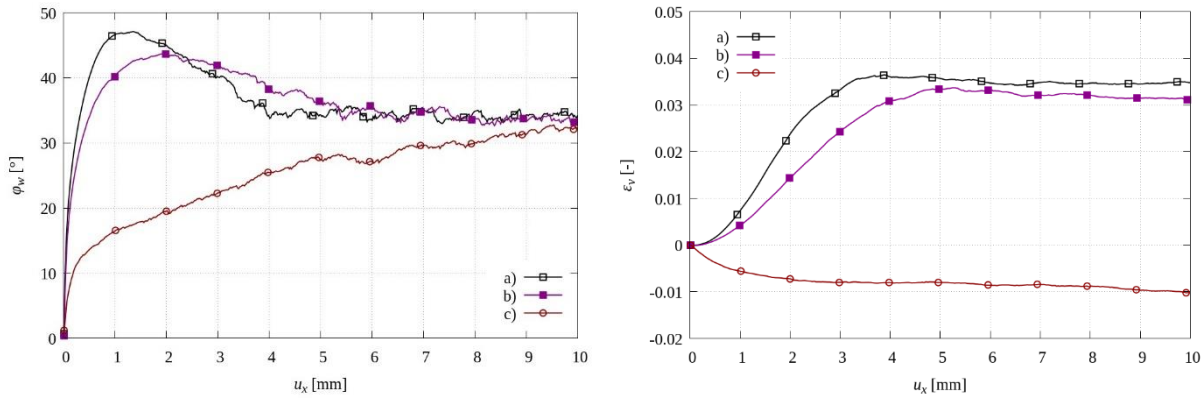

Fig. 4: Internal friction angle φ_W and volumetric strain ε_V versus horizontal displacement u_x from discrete simulations of direct shear test for different initial void ratios: a) $e_0 = 0.53$, b) $e_0 = 0.63$ and c) $e_0 = 0.75$ ($\sigma_0 = 200$ kPa)

FIGURE 4

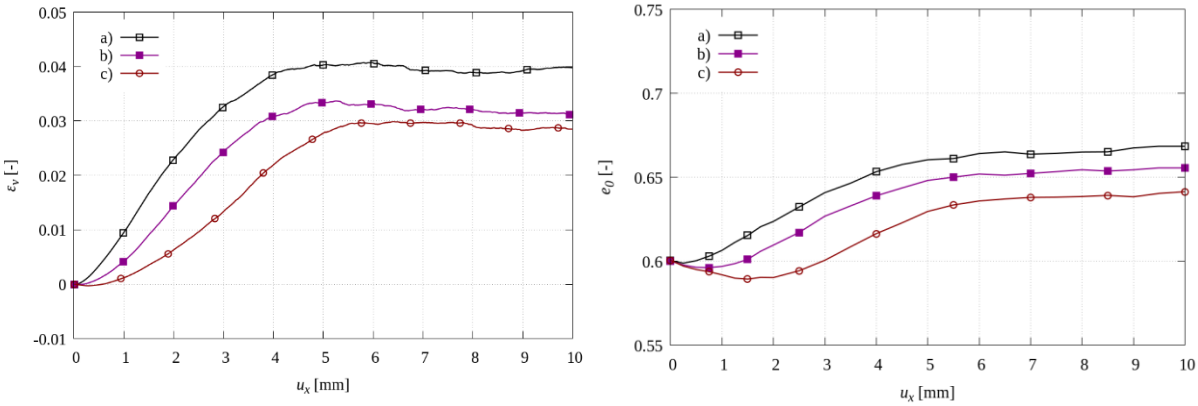

Fig. 5: Internal friction angle φ_w and volumetric strain ε_v versus horizontal displacement u_x from discrete simulations of direct shear test for different vertical load: a) σ_0 = 50 kPa, b) σ_0 = 200 kPa and c) σ_0 = 500 kPa (e_0 = 0.63)

FIGURE 5

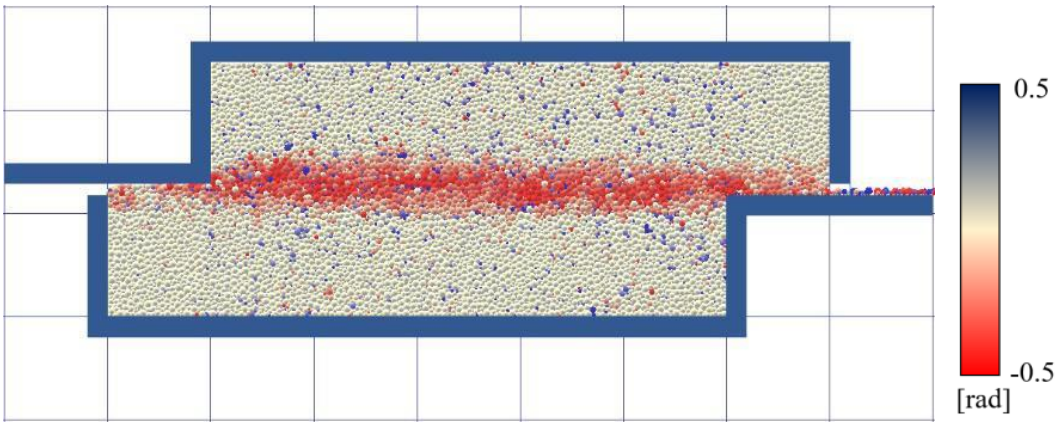

Fig. 6: Exemplary distribution of sphere rotation at the final stage of the direct shear test (red colour – clockwise rotations, blue colour – anti-clockwise rotations) *(colour online)*

FIGURE 6

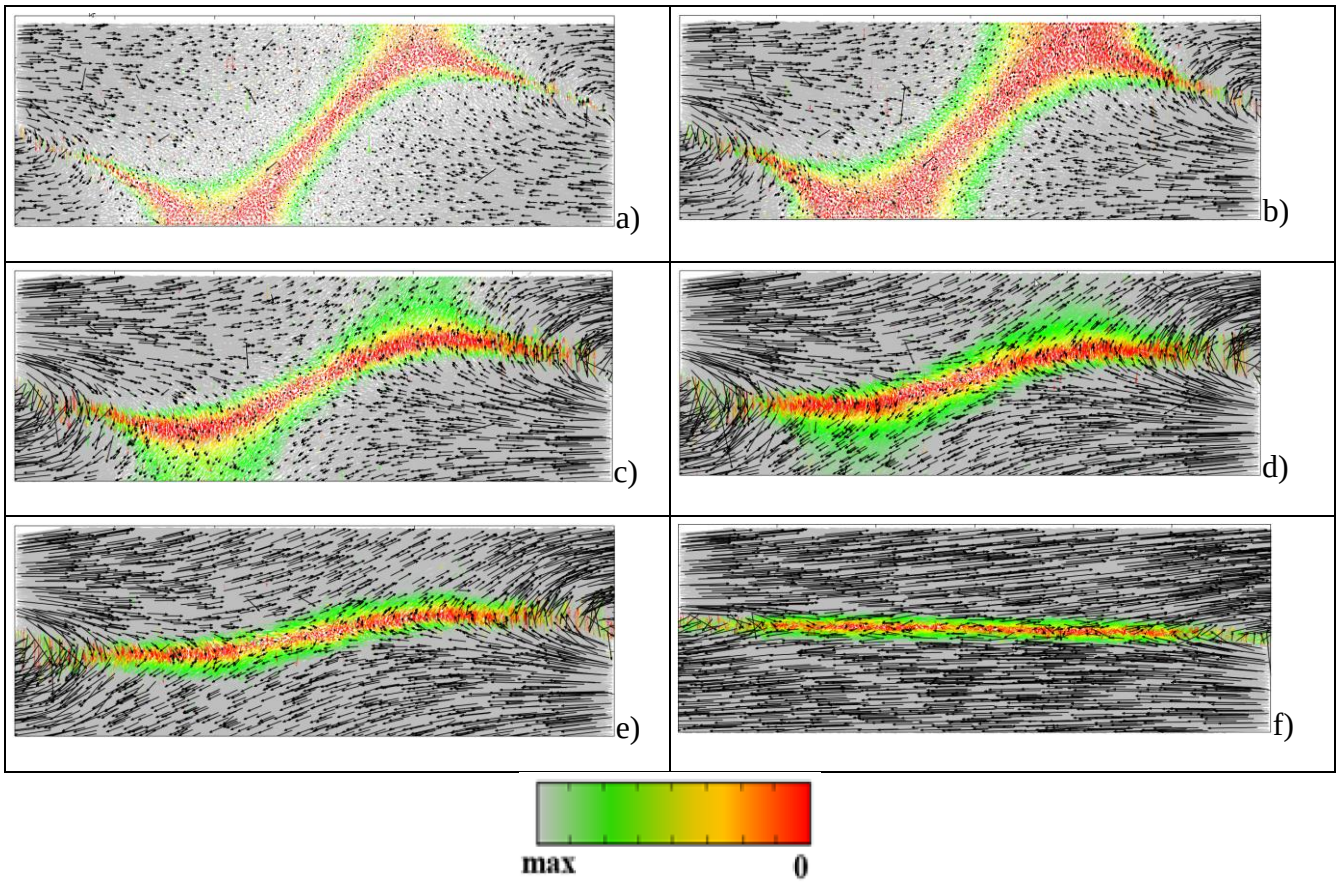

Fig. 7: Evolution of displacements fluctuations ($\vec{u}_i - \vec{u}_{avg}$) in the entire specimen for: a) u_d = 0.10 mm, b) u_d = 0.50 mm, c) u_d = 1.00 mm, d) u_d = 1.50 mm, e) u_d = 2.00 mm and f) u_d = 7.00 mm (e_0=0.63, σ_0=200 kPa, d_{50}=0.5 mm) (arrows are multiplied by 1e03 due to readability) (grey and red colour correspond to the maximal and minimal fluctuations' value, respectively) (black arrows shows every 50 elements only)

FIGURE 7

1

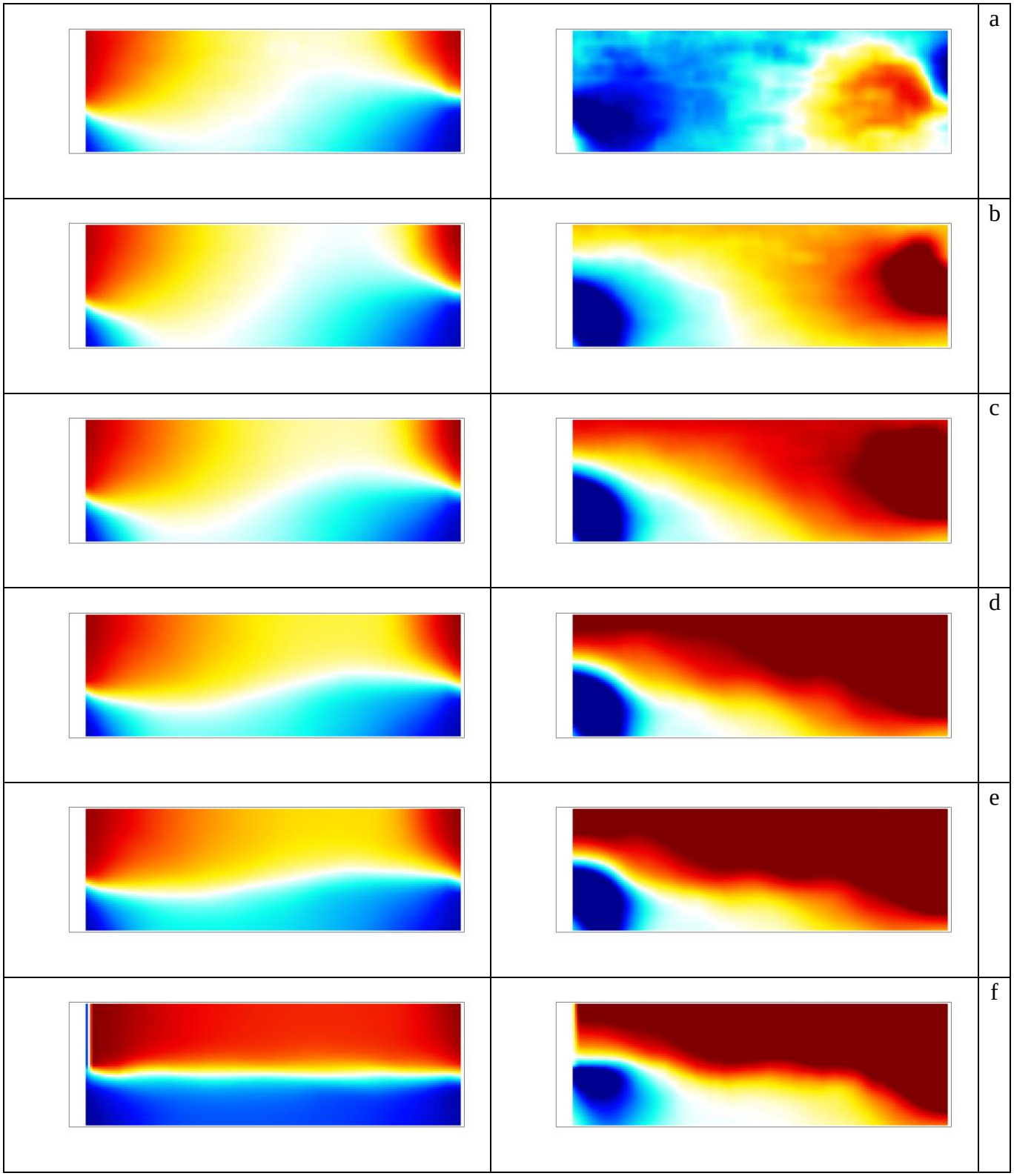

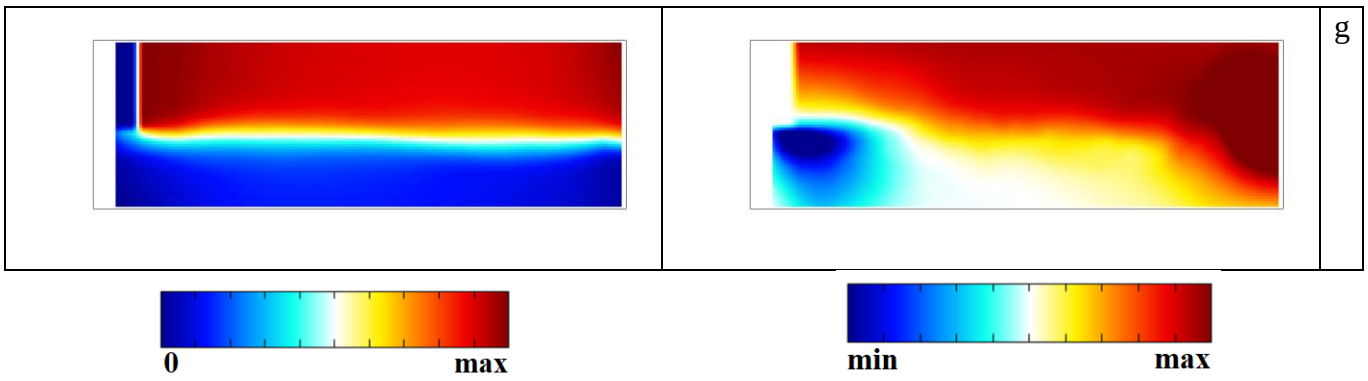

A) B)

Fig.8: Evolution of displacements: A) u_x' (horizontal) and B) u_y' (vertical) in the entire specimen for: a) u_x=0.10 mm, b) u_x=0.50 mm, c) u_x=1.00 mm, d) u_x=1.50 mm, e) u_x=2.00 mm, f) u_x=5.00 mm and g) u_x=7.00 mm (red colour denotes positive displacement, blue colour denotes negative displacement) *(colour online)*

FIGURE 8

1

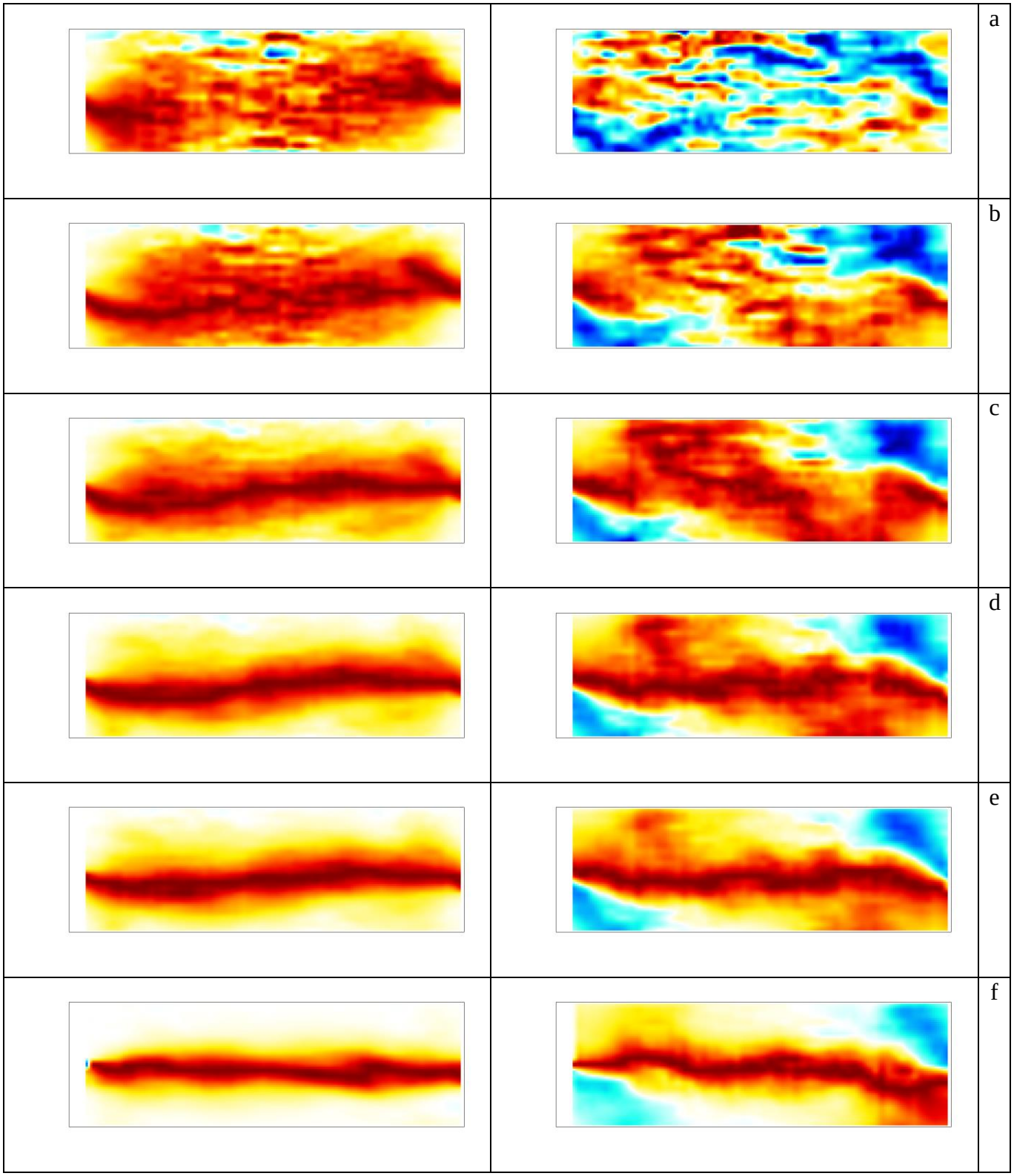

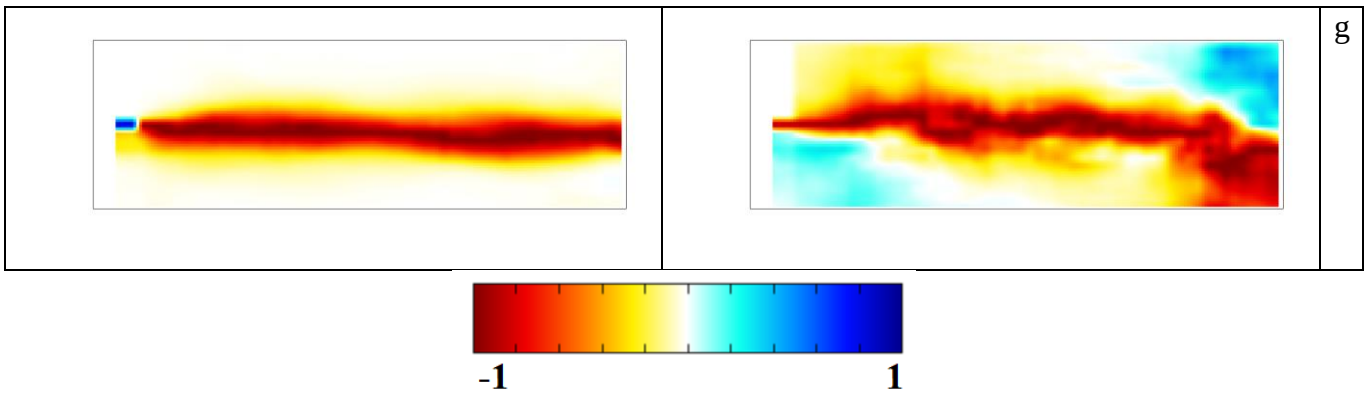

Fig.9: Evolution of the gradient of displacements: A) u_x* (horizontal) and B) u_y* (vertical) in the entire specimen for: a) u_x=0.10 mm, b) u_x=0.50 mm, c) u_x=1.00 mm, d) u_x=1.50 mm, e) u_x=2.00 mm, f) u_x=5.00 mm and g) u_x=7.00 mm (blue colour denotes increase, red colour denotes decrease) *(colour online)*

FIGURE 9

1

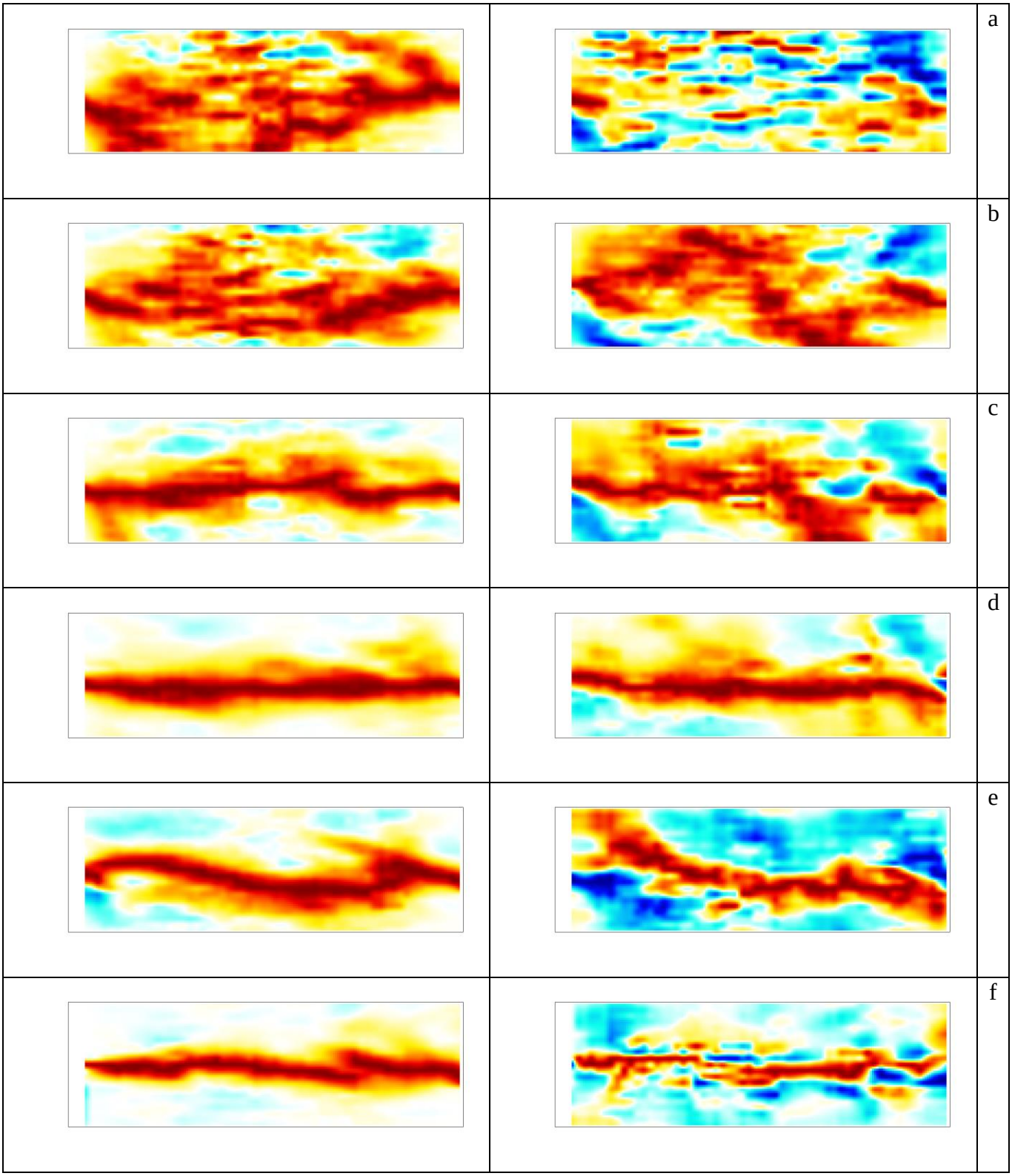

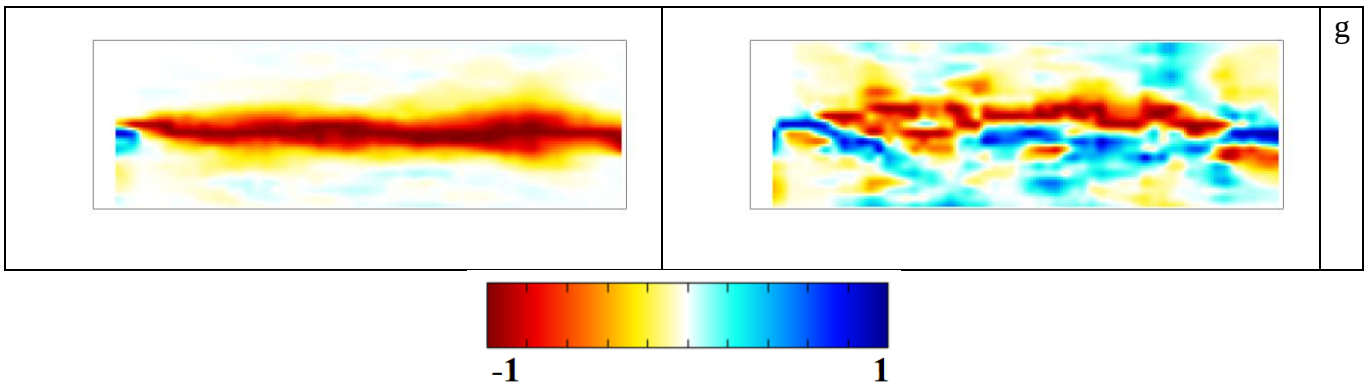

A) B)

Fig.10: Evolution of gradient of velocities: A) v_x (horizontal) and B) v_y (vertical) in the entire specimen for: a) u_x=0.10 mm, b) u_x=0.50 mm, c) u_x=1.00 mm, d) u_x=1.50 mm, e) u_x=2.00 mm, f) u_x=5.00 mm and g) u_x=7.00 mm (red colour denotes increase, blue colour denotes decrease) *(colour online)*

FIGURE 10

1

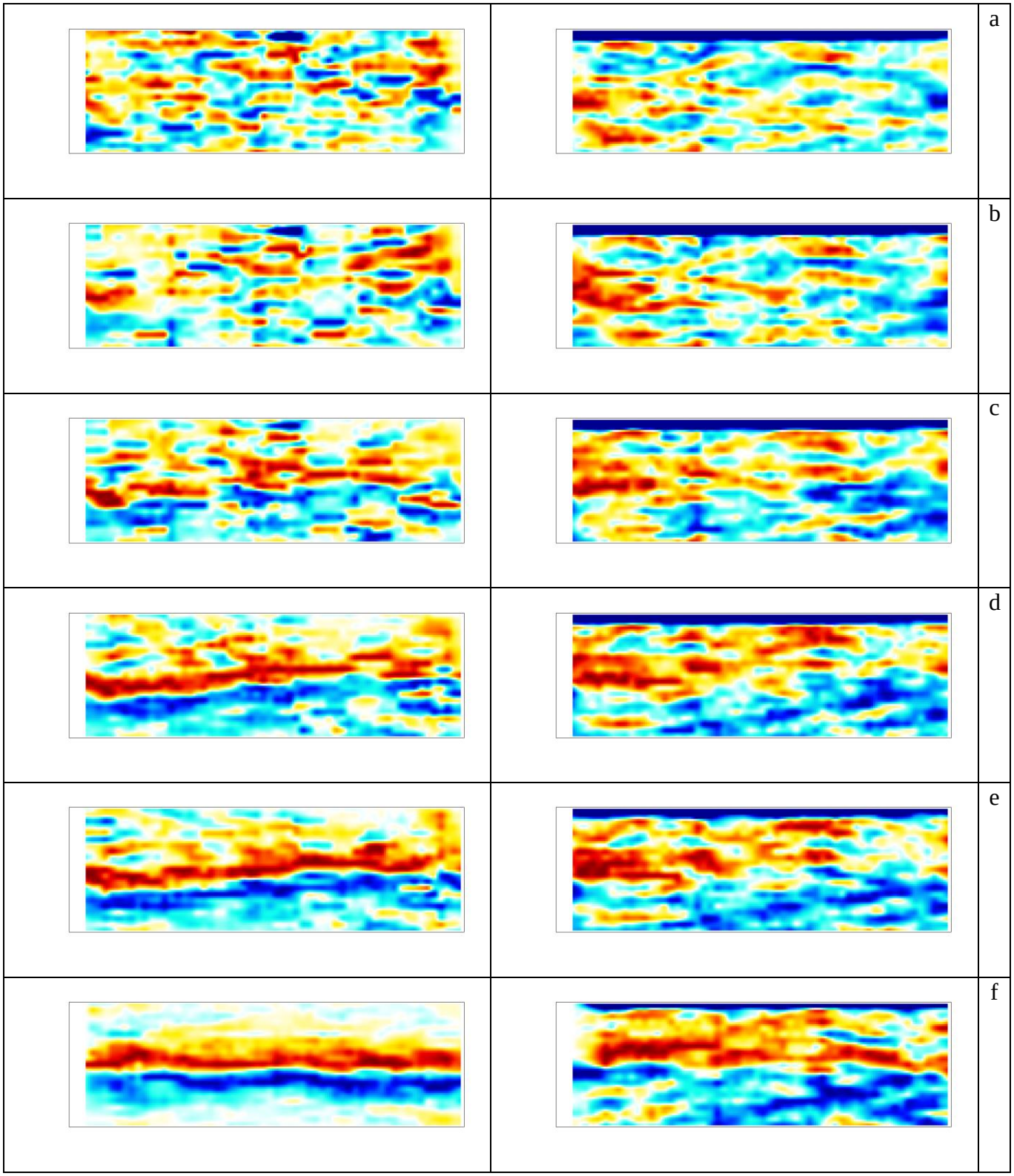

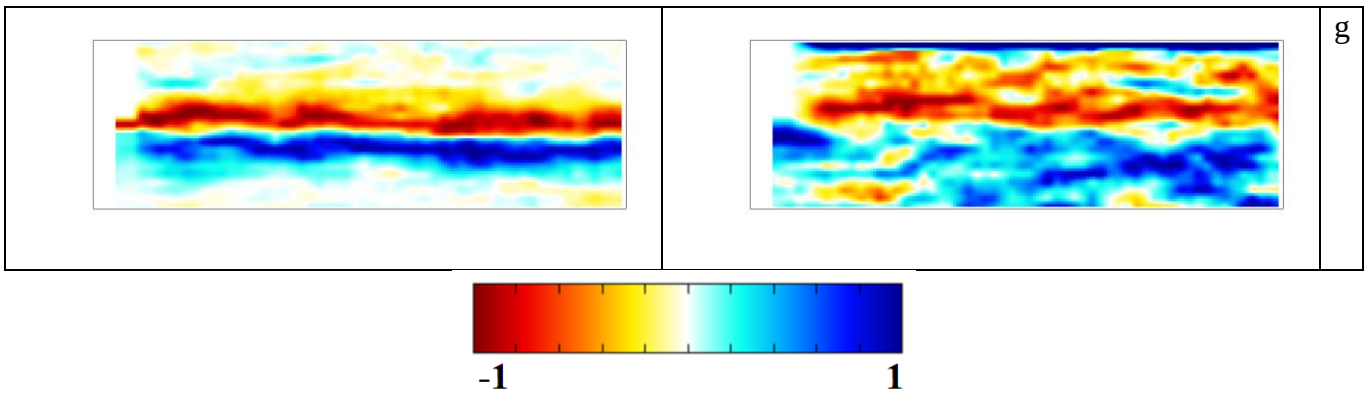

A) B)

Fig.11: Evolution of gradient of A) rolling and B) contact number in the entire specimen for: a) u_x=0.10 mm, b) u_x=0.50 mm, c) u_x=1.00 mm, d) u_x=1.50 mm, e) u_x=2.00 mm, f) u_x=5.00 mm and g) u_x=7.00 mm (red colour denotes increase, blue colour denotes decrease) *(colour online)*

FIGURE 11

1

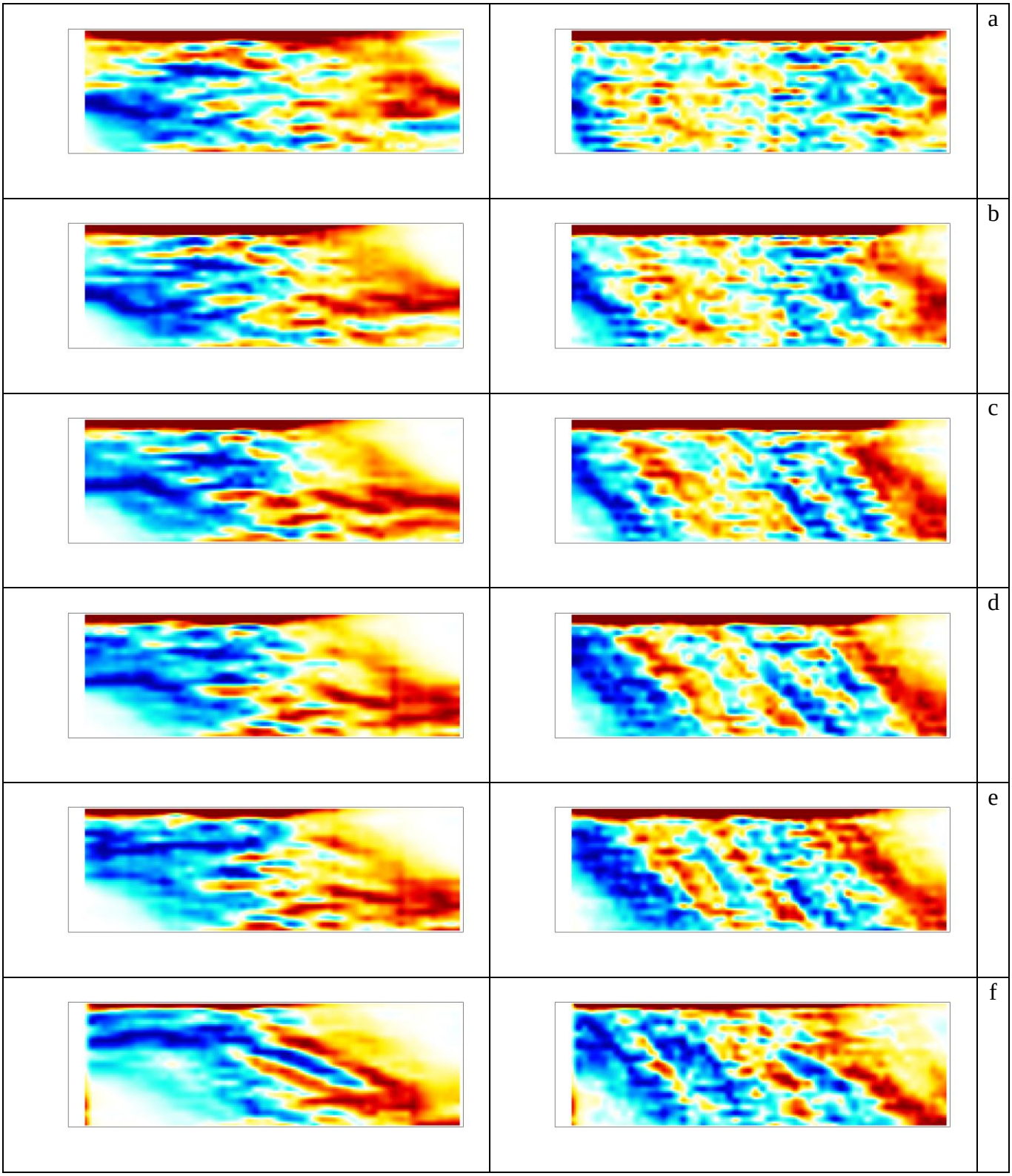

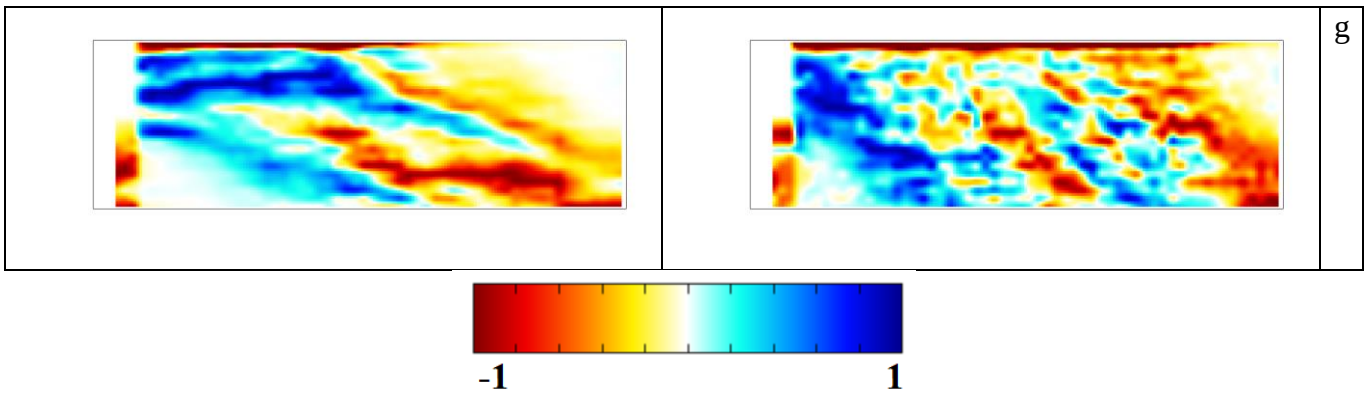

A) B)

Fig.12: Evolution of gradient of stresses A) σ_{xx} and B) σ_{yy} in the entire specimen for: a) u_x=0.10 mm, b) u_x=0.50 mm, c) u_x=1.00 mm, d) u_x=1.50 mm, e) u_x=2.00 mm, f) u_x=5.00 mm and g) u_x=7.00 mm (red colour denotes increase, blue colour denotes decrease) *(colour online)*

FIGURE 12

1

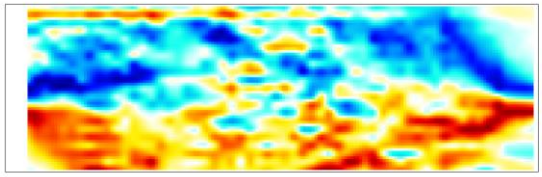	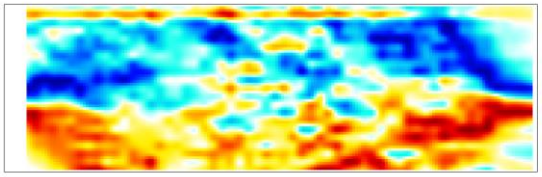	a
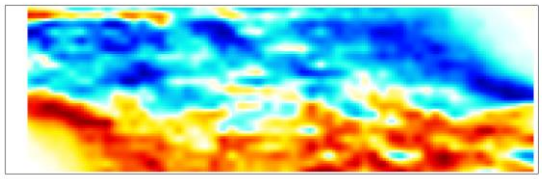	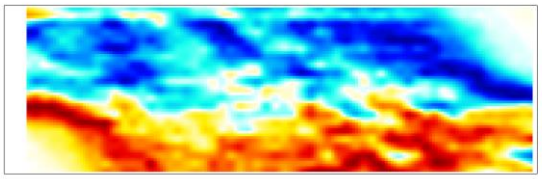	b
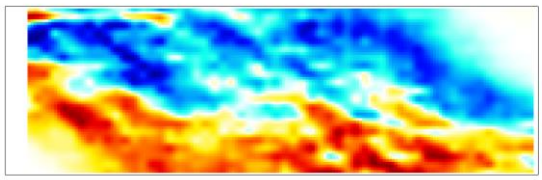	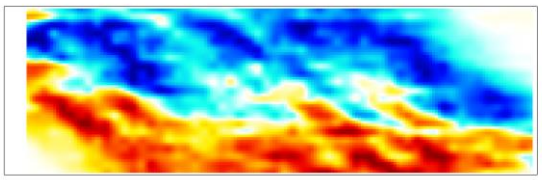	c
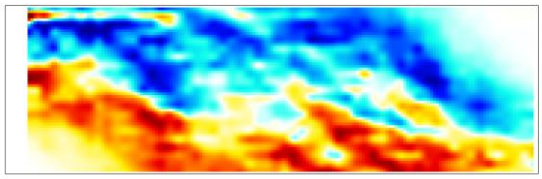	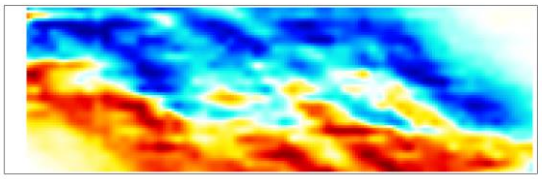	d
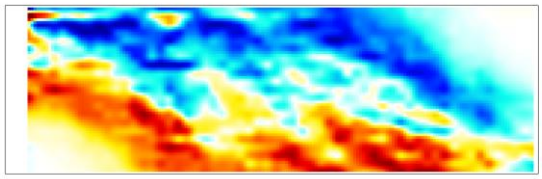	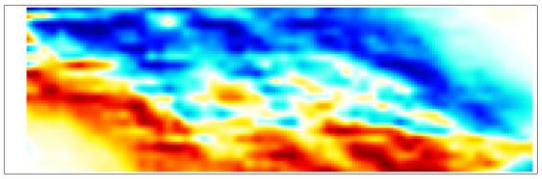	e
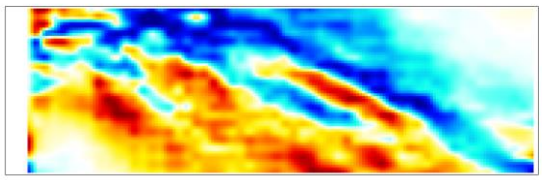	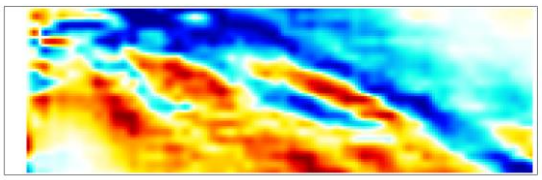	f

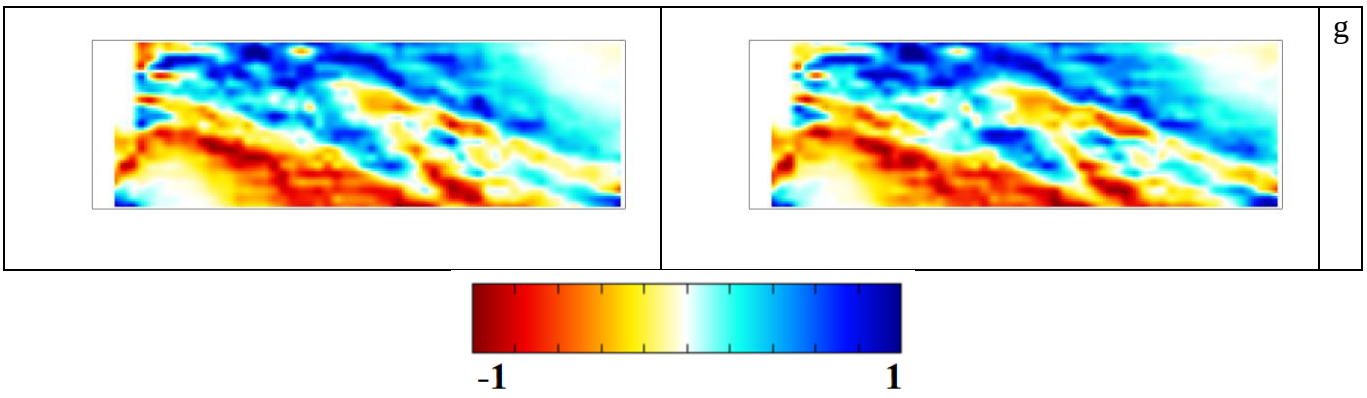

Fig.13: Evolution of gradient of stresses A) σ_{yx} and B) σ_{yx} in the entire specimen for: a) u_x=0.10 mm, b) u_x=0.50 mm, c) u_x=1.00 mm, d) u_x=1.50 mm, e) u_x=2.00 mm, f) u_x=5.00 mm and g) u_x=7.00 mm (red colour denotes increase, blue colour denotes decrease) *(colour online)*

FIGURE 13

1

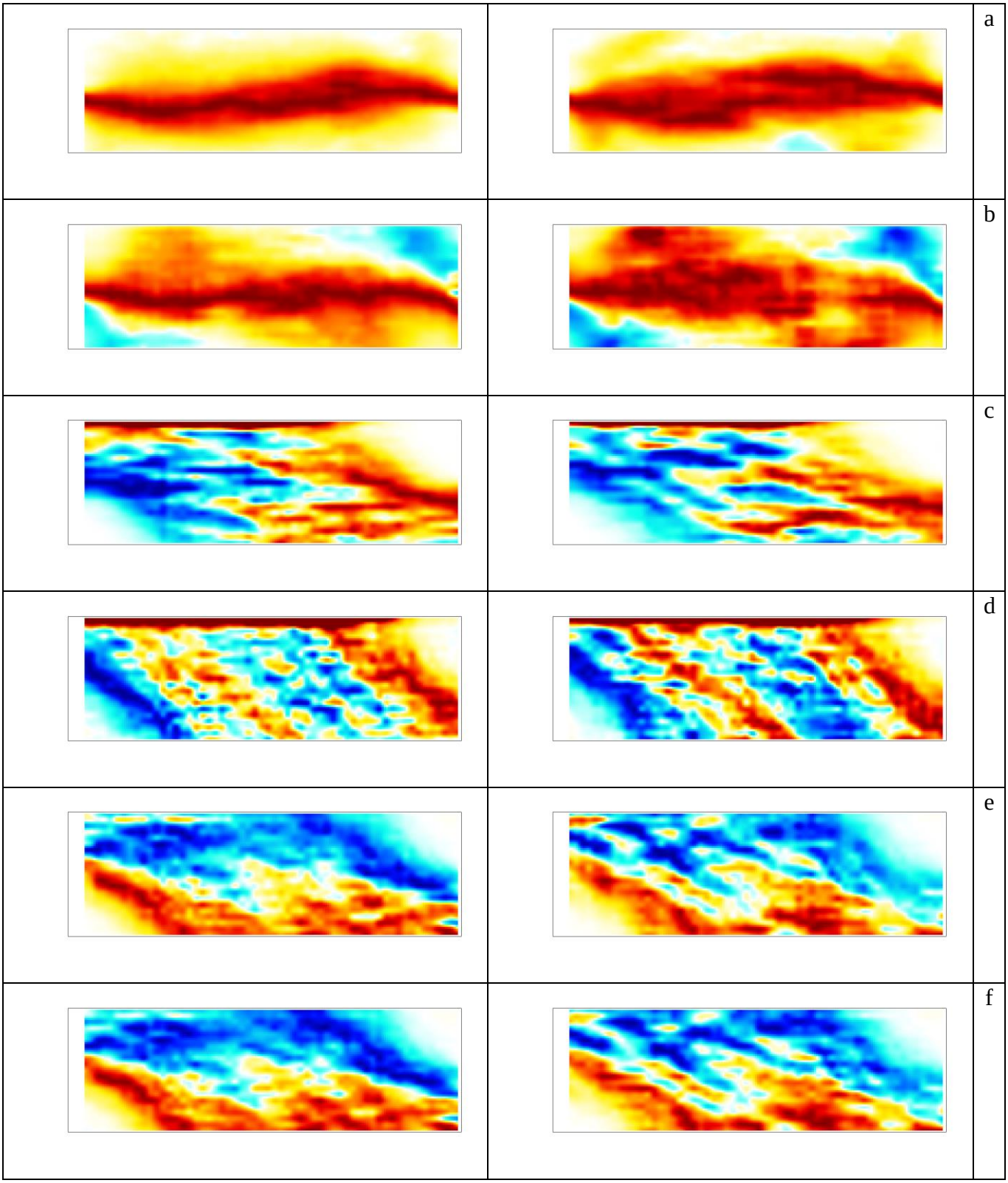

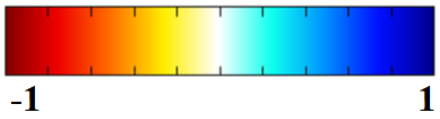

A) B)

Fig.14: Maps of gradient for specimen with initial pressure equal: A) σ_0 = 50 kPa and B) σ_0 = 500 kPa for entire specimen for u_x=1.00 mm: a) horizontal displacement (u_x*) b) vertical displacement (u_y*), c) horizontal stresses (σ_{xx}), d) vertical stresses (σ_{yy}), e) shear stresses (σ_{xy}) and f) shear stresses (σ_{yx}) (red colour denotes increase, blue colour denotes decrease) *(colour online)*

FIGURE 14

1

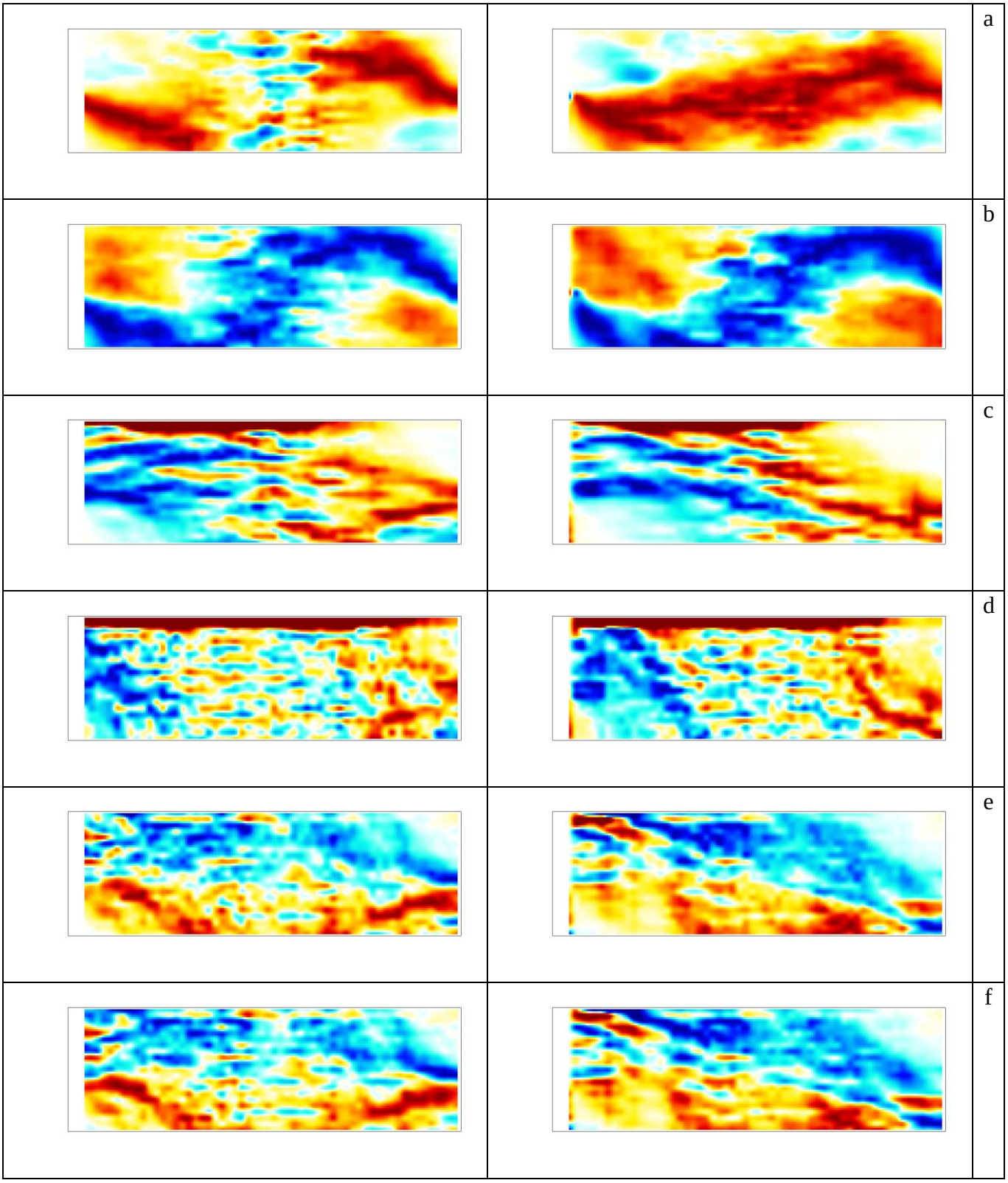

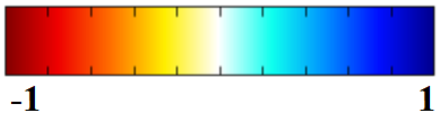

A) B)

Fig.15: Maps of gradient for initial loose specimen (e_0=0.75) for entire specimen for A) u_d=1.00 mm (pre-peak) and B) u_d=5.00 mm (residual part): a) horizontal displacement (u_x*) b) vertical displacement (u_y*), c) horizontal stresses (σ_{xx}), d) vertical stresses (σ_{yy}), e) shear stresses (σ_{xy}) and f) shear stresses (σ_{yx}) (red colour denotes increase, blue colour denotes decrease) *(colour online)*

FIGURE 15